ACS APPLIED MATERIALS & INTERFACES

Research Article

www.acsami.org

Room-Temperature Fast Construction of Outperformed ZnO Nanoarchitectures on Nanowire-Array Templates for Dye-Sensitized Solar Cells

Wei-Ting Jiang, Chun-Te Wu, Yu-Hsiang Sung, and Jih-Jen Wu*

Department of Chemical Engineering, National Cheng Kung University, Tainan 701, Taiwan

Supporting Information

ABSTRACT: A ZnO nanoarchitecture composed of nanocactus (NCs) and nanosheets (NSs) is constructed on the ZnO-nanowire (NW)-array template within 4 min by a facile room-temperature (RT) chemical bath deposition (CBD) for use in dye-sensitized solar cells (DSSCs). Compared to the ZnO NW array, the spines and shells of NCs provide larger and more fitting surface for dye adsorption. The NSs developed on the top and side walls of the NWs afford the additional surface for dye adsorption as well as for light scattering. Moreover, the RT-grown ZnO nanostructures possess an upward-shifted conduction band edge and a fast electron transport rate compared to the primary ZnO NW array. With an anode thickness of 9 μm, an efficiency of 5.14% is therefore simply attained in the D149-sensitized ZnO NC-NS DSSC.

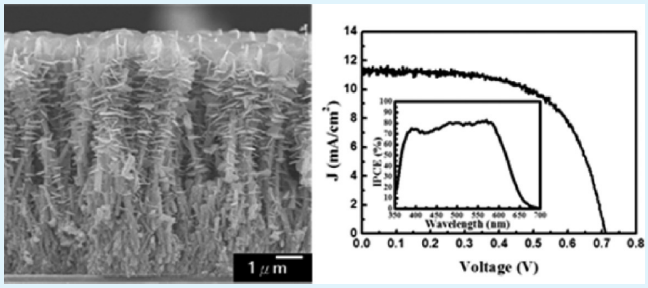

KEYWORDS: *ZnO nanowire array, room-temperature chemical bath deposition, ZnO nanoarchitecture, dye-sensitized solar cell, light scattering, electron transport*

INTRODUCTION

ZnO, which has an energy band gap similar to that of the ordinarily used TiO_2 but possesses higher electron mobility, is an alternative anode material for dye-sensitized solar cells (DSSCs).[1] However, the highest power conversion efficiency (η) of 7.5% for ZnO-based DSSC reported recently[2] is still lower than the record η of 12.3% for TiO_2-based DSSC.[3] The main reason may be that DSSC dyes are always designed for TiO_2 nanoparticle (NP) film anode whereas there is no efficient dye available for ZnO anode.[4,5]

The incident-photon-to-current efficiency (IPCE) of a DSSC can be considered as the product of light harvesting efficiency ($\eta_{LH}(\lambda)$), electron injection efficiency (ϕ_{inj}), and charge collection efficiency (η_c)

$$\mathrm{IPCE}(\lambda) = \eta_{LH}(\lambda)\phi_{inj}\eta_c \quad (1)$$

Superior electron transport properties and therefore charge collection efficiencies have been demonstrated in ZnO-based DSSCs with various anode structures, such as single-crystalline nanowire (NW),[6] porous crystalline film,[4] NW/NP composite film,[7,8] and nanodendrite/NP composite film.[9] On the other hand, the poor chemical stabilities of the ZnO electrode in the acidic dye solution[10] and in the presence of complexing agents of the dyes[11] result in ZnO deterioration and the difficulty of dye uptake, which has been reported as the most probable reason for the inferior performance of ZnO DSSC.[5] In addition, with most of the common dyes, the electron injection efficiency in the ZnO-based DSSCs is inferior to that in the TiO_2-based DSSCs, which may be mainly attributed to both low dielectric constant and low density of states in the conduction band of ZnO.[5]

Indoline dyes have been found a comparatively good match with ZnO because of its lower acidity and the lack of complexing agent.[4,5] With the high extinction coefficient, the efficiencies of the ZnO-based DSSC above ~5% can be attained using the indoline dye coded D149.[4,12] However, the absorption wavelengths of D149 dye is limited within the visible light range which is much narrower than that of ruthenium dye.[4] The narrow absorption range may restrict the efficiency of the D149-sensitized ZnO DSSCs. With the absence of dyes specially designed for ZnO anodes, ZnO nanostructures still attract considerable attention for solar cell application because of its low crystallization temperature and anisotropic growth behavior[1] in addition to superior electron transport properties. Enhancement of the performances of the ZnO-based DSSC can be realized by utilizing the variety of ZnO nanostructures.[7−9,13]

To increase the light harvesting efficiency of the ZnO NW DSSC, the strategies of modifications of the ZnO NW arrays have been reported by enlarging the surface area of photoanode without sacrificing fast electron transport of ZnO NW[7−9] and adding a light scattering layer for reflecting unabsorbed photons

Received: November 4, 2012
Accepted: January 8, 2013
Published: January 8, 2013

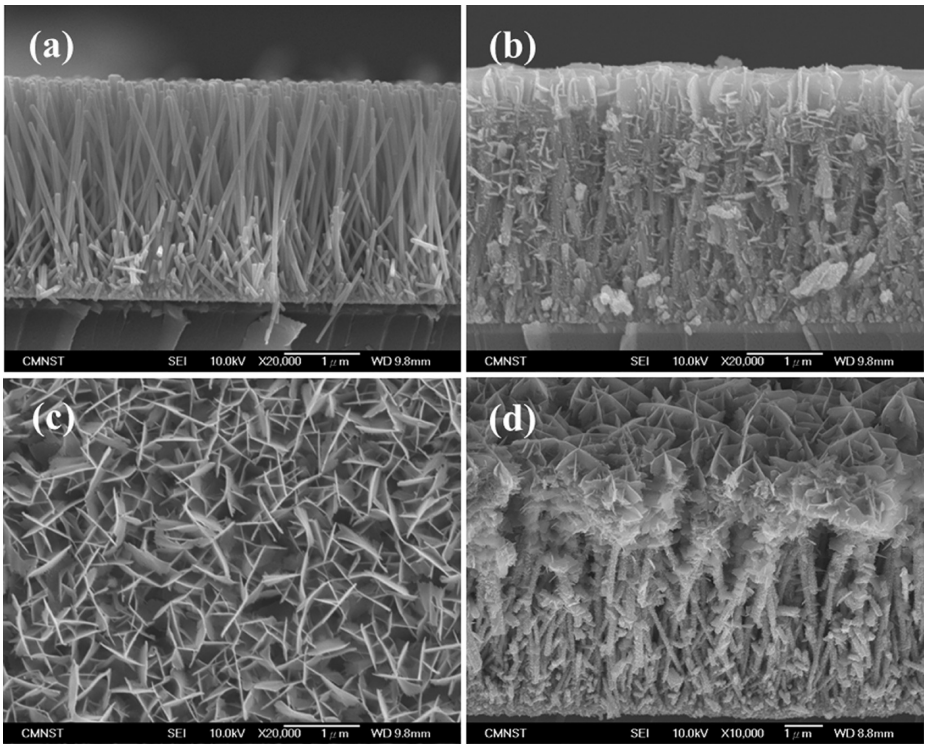

Figure 1. (a) Cross-sectional SEM image of ZnO NW array on ITO substrate. (b) Cross-sectional, (c) top-view, and (d) 45°-tilted SEM images of ZnO NC-NS frameworks.

back into the NW anode.[14] In the present work, an outperformed ZnO nanoarchitecture that is synthesized on the ZnO NW-array template at room-temperature (RT) is demonstrated to satisfy the aforementioned concepts simultaneously. We have reported the RT chemical bath deposition (CBD) of hierarchical nanostructures on ZnO NWs and nanoneedles to respectively construct ZnO nanocactus (NC) array[13] and nanosheet (NS) framework[15] for use in dye-sensitized and hybrid polymer solar cells. Significantly, enhancements of the photovoltaic performances are attained through the modifications of the primary ZnO nanostructures simply by RT CBD. A new version of RT-grown ZnO nanoarchitecture composed of both NS and NC is constructed on the ZnO-NW-array template by one-pot synthesis within 4 min in this work. The RT NC-NS frameworks constructed on ZnO-NW-array templates, which exhibit large surface area, high light scatter ability, upward-shifted conduction band edge and fast electron transport rate, are demonstrated to be an efficient anode of DSSCs. With an anode thickness of 9 μm, an efficiency of 5.14% is therefore simply attained in the D149-sensitized ZnO NC-NS DSSC.

EXPERIMENTAL SECTION

ZnO NW arrays were grown on seeded indium tin oxide (ITO) substrates by CBD in a 0.02M aqueous solution of zinc acetate ($Zn(CH_3COO)_2{\cdot}2H_2O$, ZnAc·$2H_2O$, Merk, 99.5 %) and hexamethylenetetramine ($C_6H_{12}N_4$, HMTA, Riedel-de Haen, 99.5 %) at 95 °C. The seed layers were prepared by the spin coating of a methanolic solution of ZnO NPs on the ITO substrates followed by annealing at 350°C for 10 min. To synthesize the ZnO NPs,[16] a 65 mL of methanolic solution of 0.03 M NaOH was added dropwise into a 125 ml of methanolic solution of 0.01 M zinc acetate at 60 °C under vigorous stirring and the solution was kept stirring for 2 h at 60 °C. For construction of the ZnO NS-NS frameworks on ZnO NWs, the ZnO NW array/ITO substrate was immersed in a vigorously stirred (1250 rpm) aqueous solution of 0.062 M zinc acetate and 0.455 M NaOH at RT. The morphologies of the ZnO nanostructures were examined using scanning electron microscopy (SEM, JEOL JSM-7000F). Structural characterizations of the ZnO nanostructures were performed using transmission electron microscopy (TEM) (JOEL 2100F and FEI E.O Tecnai F20 G2MAT S-TWIN). Optical properties of the ZnO nanostructures were measured using a UV-Vis-IR spectrophotometer (JASCO V-670).

Dye adsorption was carried out by immersing the anode in a 5 x 10^{-4} M acetonitrile/t-butanol (1:1) solution of D149 at room temperature for 40 min. The sensitized electrode and platinized FTO counter electrode were sandwiched together with 25-μm-thick hot-melt spacers (SX 1170-25, Solaronix SA). Liquid electrolyte solutions composed of 0.5 M tetrapropylammonium iodide (TPAI) and 50 mM I_2 in a 1:4 volume ratio of ethylene carbonate and acetonitrile was employed for the D149-sensitized DSSCs. Photovoltaic properties of the DSSCs were measured under AM 1.5 simulated sunlight at 100 mW cm^{-2} (300 W, Model 91160A, Oriel). A mask was used to create an exposed area of 0.16 cm^2 for all cells. The amount of dye adsorption was determined by measuring the optical absorbance of the photoanode at 526 nm.[13]

IPCE spectra were measured using 500 W xenon light source (Oriel) and a monochromater (Oriel Cornerstone) equipped with Si (Model 71640, Oriel) detector. Intensity modulated photocurrent spectroscopy (IMPS) and intensity modulated photovoltage spectroscopy (IMVS) measurements were conducted under a modulated green LED light (530 nm) driven by a source supply (Zahner, PP210) and a potentiostat (Zaher, IM6ex) with a frequency response analyzer (FRA). The experimental procedure and the method for extraction of electron transit times of the DSSCs from the IMPS and IMVS responses have been described in detail elsewhere.[8]

RESULTS AND DISCUSSION

Figure 1a shows the aligned ZnO NWs grown on the seeded ITO substrates by CBD. The average diameter and thickness of the NWs are 60 nm and 2.8 μm, respectively. The density of the NWs is ~6x10^9 cm^{-2}. The nanoarchitectures composed of spines and NSs are further constructed on the ZnO NWs

simply by immersing the ZnO NW array/ITO substrate in the stirring supersaturated aqueous solution of ZnAc and NaOH at RT for 2 min. As shown in Figure 1b–d, the diameters of NWs are increased to 90–120 nm and many spines are grown on the side walls of the NWs to form the NC array.[13] In addition, NSs in sizes of ~ hundreds nm are also developed from the side walls and the top of the ZnO NWs. The ZnO NC-NS frameworks with a thickness of 3.3 μm are consequently constructed based on the ZnO NW arrays on ITO substrates using the RT CBD. It is worth addressing here that the versatile hierarchical nanostructures, including ZnO NC array,[13] ZnO NS framework[15] and ZnO NC-NS framework, developed from the one-dimensional ZnO nanostructures are attainable using the RT CBD by varying the concentration of the aqueous solution of ZnAc and NaOH as well as the stirring speed during process.

The structure of the NCs composed of shells and spines has been investigated by TEM in the previous work.[13] The shell is epitaxially grown on the surface of the primary the NW and the spine is developed from the etch pit on the ZnO NW during the RT CBD. In the present work, the structures of NSs developed from the top and side walls of ZnO NW are further examined by TEM. Figure 2a shows a typical TEM image of the ZnO NS on the top of ZnO NW scratched form the ZnO NC-NS frameworks. The selected area electron diffraction (SAED) pattern of the ZnO NW, as displayed in Figure 2b, shows that the single-crystalline structure of the ZnO NW is sustained after the RT CBD process. The SAED pattern of the interfacial region between NW and NS is shown in Figure 2c. It reveals that some extra spots appear in the SAED pattern in addition to the diffraction spots of ZnO single crystal, suggesting that the defects exist at the interfacial region connecting NS and NW. Figure 2d illustrates the high-resolution (HR) TEM image of the NS. It reveals that ZnO NS formed on the top of NW also possesses single-crystalline structure. The growth direction of NS is along [0001], which is parallel to that of NW.

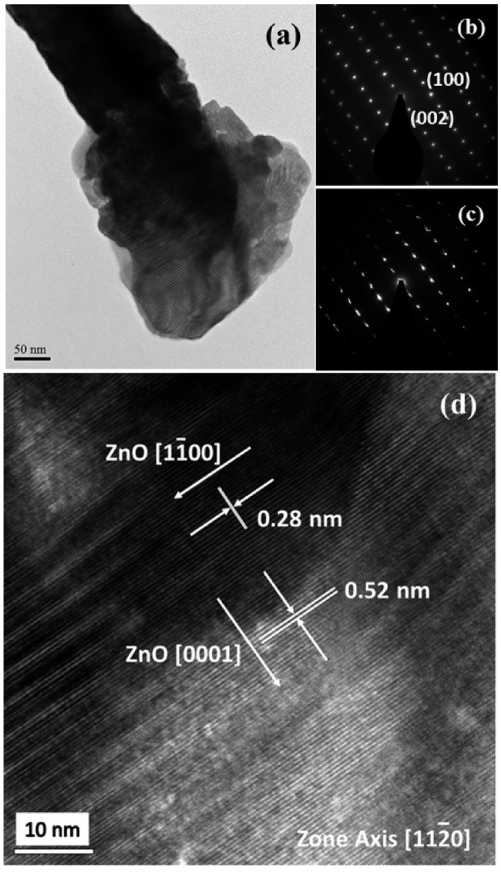

Figure 2. (a) TEM image of ZnO NS on the top of ZnO NW. (b) and (c) SAED patterns of ZnO NW and NW/NS interfacial region, respectively. (d) HRTEM image of NS.

TEM characterizations show that there are at least two types of NSs developed from the side walls of ZnO NWs. Figure 3a shows the first type of the NS on the side wall of ZnO NW, which 2D feature is recognizable in the TEM image. The HRTEM image taken at the interfacial region of the NS and NW, as shown in Figure 3b, indicates that the ZnO NS possesses single-crystalline structure and is epitaxially developed from the side wall of ZnO NW. The homoepitaxial relationship between the NS and NW is further confirmed by the SAED pattern in which only one single-crystalline diffraction pattern appears as displayed in Figure 3c. TEM characterizations of another type of NS with the 2D feature almost parallel to the incident electron beam are shown in Figure 4. Figure 4a displays the TEM image of the NW with short spines and edge-view NSs. The HRTEM image of the NW and NS, which is taken with the same zone axis of [11$\bar{2}$0] for both NW and edge-view NS, is shown in Figure 4b. It reveals that the angle between the [0001] directions of NW and NS is ~110°. The nano-beam diffraction patterns taken form the NW and NS are respectively shown in panels c and d in Figure 4, indicating the single crystal structures of NW and NS. Figure 4(b) shows that the exposure surface of the ZnO NS is (1$\bar{1}$00) (m-plane). This type of NS developed from the side wall of NW, which the 2D feature exposes with a small angle to

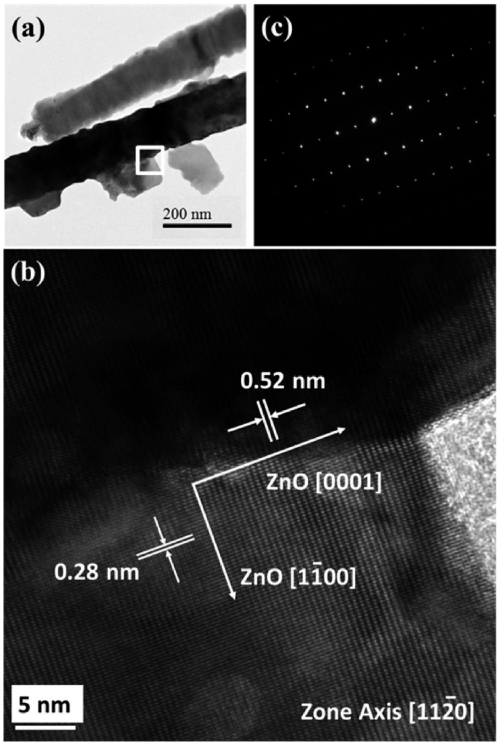

Figure 3. (a) TEM image of ZnO NSs on the side wall of ZnO NW. (b) HRTEM image and (c) SAED pattern of the interfacial region of ZnO NW and NS denoted in a.

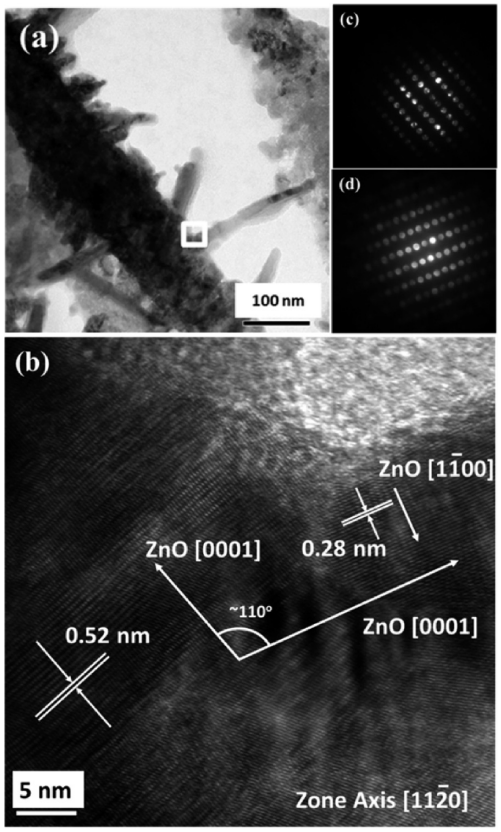

Figure 4. (a) TEM image of the NW with short spines and edge-view NSs. (b) HRTEM image of the interfacial region of ZnO NW and NS denoted in a. (c, d) Nano-beam diffraction patterns of ZnO NW and NS, respectively.

the vertical NW, may play a role in the reflection of the incident light passing through the interstices of NWs.

The ZnO NC-NS frameworks were employed as the anodes to fabricate DSSCs. Current density (J)−voltage (V) curve of the D149-sensitized ZnO NC-NS DSSC is shown in Figure 5.

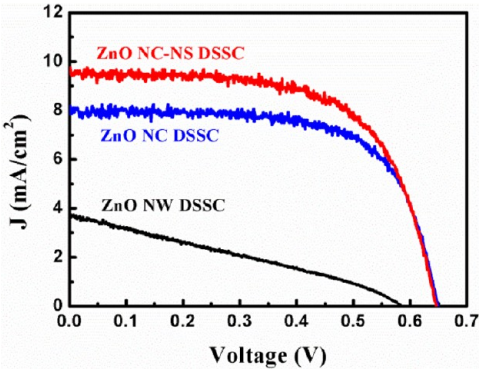

Figure 5. J−V curves of the D149-sensitized ZnO NW, ZnO NC, ZnO NC-NS DSSCs.

For comparison, the J−V curve of the D149-sensitized NW DSSC is also illustrated in this figure. The photovoltaic properties of the cells are listed in Table 1. It shows that with an anode thickness of 2.8 μm, the ZnO NW DSSC possesses an efficiency (η) of 0.65% which is inferior to that (1.82%) demonstrated in our previous work.[13] It should be noted here that in order to fabricate high-density NW array for

Table 1. Photovoltaic Properties of ZnO NW, NC, and NC-NS DSSCs

DSSC	V_{oc} (V)	J_{sc} (mA cm^{-2})	FF	η (%)	dye loading (nmol cm^{-2})
ZnO NW	0.59	3.99	0.30	0.65	8.5
ZnO NC	0.65	7.94	0.69	3.55	14.5
ZnO NC-NS(-3)	0.65	9.53	0.65	4.01	16.7
ZnO NC-NS-9	0.71	11.22	0.64	5.14	

subsequently constructing the hierarchical nanostructure, the seed layer on ITO substrate for ZnO NW growth in the present work is different from that prepared in the previous work,[13] which may results in the significant distinction in the performances of these two ZnO NW DSSCs. Nevertheless, we found that the performance of the ZnO NC DSSC fabricated using a ZnO NC anode constructed from the new ZnO NW array, as also shown in Figure 5 and Table 1, is comparable to that demonstrated in our previous work.[13] It is therefore concluded that for the application to DSSC anodes, the ZnO NW array can play a sole role as a template for developing the RT hierarchical nanostructures, such as shells, spines and NSs to form the ZnO NC and NC-NS arrays. With the well-developed RT-grown ZnO structures fully covering ZnO NWs, the performances of the ZnO NC and ZnO NC-NS anodes are not relevant to the nature of their primary structures of the ZnO NW arrays. As listed in Table 1, the short-circuit current density (J_{sc}) of the ZnO NC-NS DSSC is superior to those of the ZnO NW and NC DSSCs. A DSSC efficiency of 4.01% is achieved using the ZnO NC-NS anode simply by the formation of hierarchical nanostructure on the 2.8-μm-thick ZnO NW anode by RT CBD for 2 min. The high Jsc may be partially attributed to the larger surface area of the NC-NS anode for dye adsorption, which is confirmed by the measurements of dye loadings as shown in Table 1 as well. Near 2-fold enhancement of the amount of dye adsorption on the ZnO anode is attained simply by the hierarchical nanostructures formed at RT for 2 min. Figure 6a shows the diffuse reflectance spectra of the ZnO NW array and ZnO NC-NS framework. The reflectance of the ZnO NC-NS framework which possesses NSs in size of ~hundreds nm on the top and within the interstices of NW array is enhanced compared to that of the ZnO NW array, as shown in Figure 6a. It reveals that in addition to the enrichment of surface area for dye adsorption, the light scattering ability of the ZnO NW photoanode is improved in the wavelength range of 400−700 nm by constructing the hierarchical nanostructure simply using RT CBD.

The IPCE spectra of the ZnO NW and ZnO NC-NS DSSCs are shown in Figure 6b. It reveals that the conversion efficiencies of the ZnO NC-NS DSSC are saturated at ~80 % in the wavelengths ranging from 480 to 550 nm (the details of which will be discussed later). The IPCE values of the ZnO NC-NS DSSC are significantly increased in the wavelengths ranging from 400 to 700 nm compared to those of the ZnO NW DSSC, which confirms the considerable enhancement of Jsc after the formation of RT nanoarchitecture on the ZnO NW anode. As shown in Figure 6b, the dissimilar features of the IPCE spectra of ZnO NC-NS and NW DSSCs suggest that the enhanced J_{sc} in ZnO NC-NS DSSC is not only from the larger amount of adsorbed dyes. In comparison with the ZnO NW DSSC, a broad feature in which the photocurrent onset extends from 640 to 700 nm is observed in the IPCE spectrum of the

dx.doi.org/10.1021/am302570r | ACS Appl. Mater. Interfaces 2013, 5, 911−917

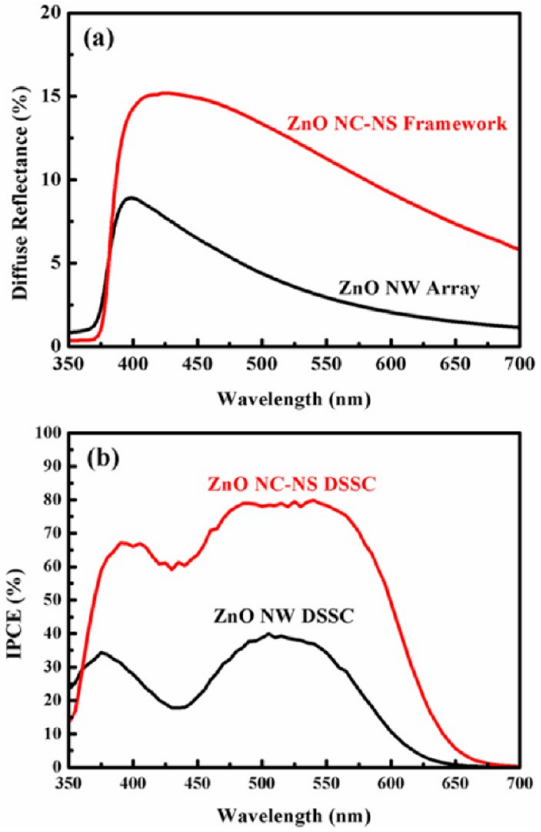

Figure 6. (a) Diffuse reflectance spectra of ZnO NC-NS framework and ZnO NW array. (b) IPCE spectra of ZnO NW and ZnO NC-NS DSSCs.

ZnO NC-NS DSSC. It indicates the efficient light scattering by the NSs occurring in the ZnO NC-NS DSSC for the photocurrent enhancement as well, which is consistent with the results of diffuse reflection measurements shown in Figure 6a.

Dynamics of electron transport and recombination in the ZnO NW, NS and NS-NC DSSCs were investigated using IMPS and IMVS, respectively. Typical IMPS responses of the three DSSCs are shown in Figure S1 (see the Supporting Information). Light intensity dependence of electron transit times are shown in Figure 7. The electron transit times in the ZnO NC-NS anodes are significantly shorter than those in the

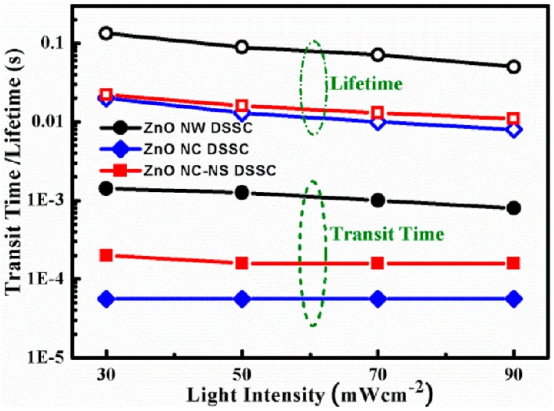

Figure 7. Dynamics of charge transport and recombination in ZnO NW, NS and NS-NC DSSCs.

ZnO NW anode, which is consistent with our previous works that the RT-grown ZnO nanostructures exhibit a superior electron transport properties than the primary ZnO NW does.[13] However, the electron transport rates in the ZnO NC-NS anode are slower than those in the ZnO NC anode. Moreover, in contrast to the ZnO NC anode with light-intensity insensitive electron transit times, as shown in Figure 7, the electron transit time in the ZnO NC-NS DSSC is insensitive to light intensity in high light intensity region but finally increase at low light intensity. It has been suggested that fewer traps exist in the RT-synthesized hierarchical nanostructures on the NWs.[13] In the ZnO NC anode, the electrons diffuse to transparent conducting oxide via the electron transport pathway of the hierarchical nanostructures instead of the primary NWs. Comparing the electron transport properties in the three anodes shown in Figure 7, it suggests that the primary NWs of the hierarchical ZnO NC-NS framework are not fully covered by shells after the 2-min RT CBD. The electron transport property in the ZnO NC-NS DSSC is therefore somewhat influenced by the template of primary NW array. Moreover, as shown in Figure 7, the IMVS measurements show that electron lifetimes in the ZnO NC-NS DSSC are shorter than those in the ZnO NW DSSC. It may be mainly ascribed to the larger surface area of the ZnO NC-NS anode, which expedites the electron recombination with the I_3^- in the electrolyte.

A thick NC-NS framework was prepared for further increasing the efficiency of ZnO NC-NS DSSC. When using an 8-μm-thick ZnO NW array as the template, the ZnO NC-NS framework with a thickness of 9 μm was formed on ITO substrate by the RT CBD, as shown in Figure 8a. It should be addressed here that the RT CBD was conducted for 4 min in this case to grow the hierarchical nanostructures fully covering the ZnO NW template. The photovoltaic performance the ZnO

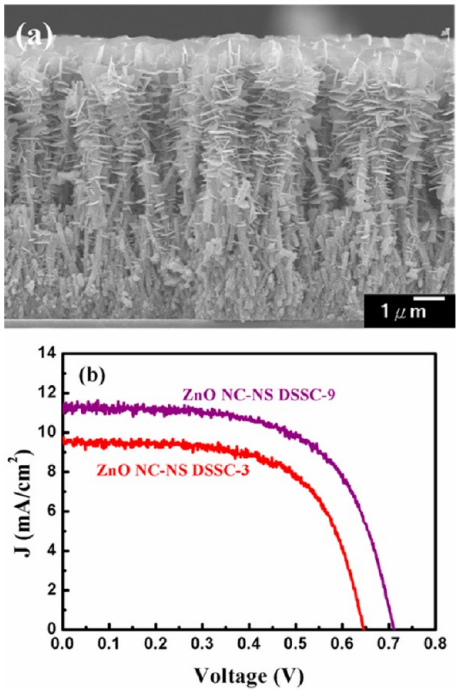

Figure 8. (a) Cross-sectional SEM image of the ZnO NC-NS framework. (b) $J-V$ curves of the D149-sensitized ZnO NC-NS DSSCs.

dx.doi.org/10.1021/am302570r | ACS Appl. Mater. Interfaces 2013, 5, 911−917

NC-NS DSSC with anode thickness of 9 μm (named as ZnO NC-NS DSSC-9 hereafter) is shown in Figure 8b. The $J-V$ curve of the ZnO NC-NS DSSC with an anode thickness of 3.3 μm (named as ZnO NC-NS DSSC-3 hereafter) is replotted in this figure for comparison. The photovoltaic properties of the cells are also listed in Table 1. They indicate that the Jsc and V_{oc} are increased when elongating the ZnO NC-NS anode. Although the increment of Jsc is not significant as expected, a DSSC efficiency of 5.14 % is achieved in the ZnO NC-NS DSSC-9 simply by the formation of hierarchical nanostructure on the 8-μm-thick ZnO NW anode at RT for 4 min.

The electron transport properties in the ZnO NC-NS DSSCs investigated by IMPS are shown in Figure 9a. The IMPS results

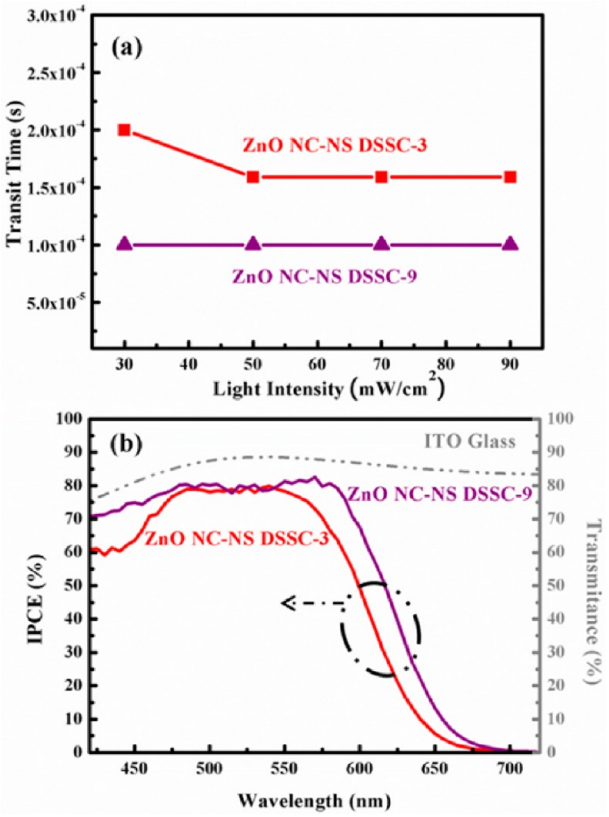

Figure 9. (a) Dynamics of charge transport in ZnO NS-NC DSSCs. (b) IPCE spectra of ZnO NC-NS DSSCs.

reveal that the electron transit times in the ZnO NS-NC-9 anode are shorter than those in the ZnO NS-NC-3 one although the anode thickness is enlogated from 3.3 μm to 9.0 μm. In addition, the electron transit times in the thicker ZnO NC-NS anode are insensitive to the light intensity. The superior electron transport property in the thicker ZnO NS-NC anode is mainly attributed to the prolonged RT CBD period compared to the thinner one for developing the RT hierarchical nanostructures fully covering the NW template in the ZnO NC-NS framework. In this case, the electrons diffuse to transparent conducting oxide via the electron transport pathway of the hierarchical nanostructures instead of the primary NWs.

Figure 9b shows the IPCE spectra of the two ZnO NC-NS DSSCs. It reveals that in the wavelength range of 480-580 nm, corresponding to the high-intensity region of the solar spectrum, the IPCE values of ZnO NC-NS DSSCs are limited to be ~80%. Equation 1 shows that the IPCE of a solar cell is governed by three factors of the light harvesting efficiency, electron injection efficiency and electron collection efficiency. As demonstrated in Figures 7 and 9a, the electron transport is rather fast in the ZnO NC-NS anodes, we suggest that the electron collection won't be an issue in the ZnO NC-NS DSSC. The light harvesting efficiency in the ZnO NC-NS DSSC is essentially restricted on the ITO transmittance as shown in this figure as well. Apart from the η_{LH} restricted by the ITO substrate with a transmittance of 85−90%, we suggest that the IPCE values in the wavelength region of 480-580 nm may also be limited by the electron injection efficiency form D149 to the conduction band of ZnO. These factors result in the limitation of IPCE values of the ZnO NC-NS DSSC-3 at ~80% in the wavelength region of 480-550 nm. When elongating the ZnO NC-NS anode from 3.3 to 9 μm, the increase of Jsc originates from the photon-electron conversion at the rest of solar spectrum, where the lights adsorbed by D149 molecules are not efficient. Therefore, the increment of Jsc is not significant in the ZnO NC-NS DSSC-9.

We have demonstrated that the RT-grown ZnO exhibits a slightly larger absorption edge than the ZnO NW array does.[15] The relative conduction band edges of the ZnO NW-based anodes with and without RT ZnO nanoarchitecture were further examined by electrochemical impedance spectroscopy (EIS) measurements conducted in the dark.[17,18] As shown in Figure S2 (see the Supporting Information), an upward shift of the conduction band edge of the ZnO anode is observed once the RT ZnO nanoarchitecture was formed on the ZnO NW array. The highest conduction band edge occurs on the hierarchical ZnO nanostructure with the RT-grown ZnO completely covering the ZnO NWs. According to the IMPS results shown in Figure 9(a), the ZnO NWs are not entirely shielded by RT ZnO in the ZnO NC-NS anode-3 whereas the well-developed RT ZnO nanostructures cover the primary ZnO NW array in the ZnO NC-NS anode-9 by prolonging the RT CBD period. The increase in the V_{oc} in the ZnO NC-NS DSSC-9 compared to that of ZnO NC-NS DSSC-3 may be attributed to the upward shift of conduction band edge of the ZnO NC-NS anode-9.

In the present work, the NC-NS nanoarchitecture which is synthesized on the ZnO NW-array template at RT for a short period within 4 min has been demonstrated to improve the light harvest efficiency by the strategies of increasing the light scattering and the dye adsorption simultaneously. The spines and shells of NCs provide more larger and fitting surface for dye adsorption. The NSs developed on the top and side walls of the NW afford the additional surface for dye adsorption as well as for light scattering. Moreover, the RT ZnO nanostructures possess an upward-shifted conduction band egde and a superior electron transport property to the primary ZnO NW array. With the characteristics of large surface area, high light-scattering ability, elevated conduction band egde and fast electron transport rate, a notable efficiency of 5.14% is therefore attained in the D149-sensitized ZnO NC-NS DSSC with an anode thickness of 9 μm. On the other hand, compared to the typical N719-sensitized TiO_2 NP DSSC, limitation of light harvesting wavelength range is a significant issue for further enhancement of the efficiency of the D149-sensitized ZnO NC-NS DSSC. We suggest that dyes specially designed for ZnO anode with wider absorption range and larger electron injection efficiency are needed to further increase the efficiency of ZnO NC-NS DSSC.

CONCLUSIONS

In this work, we demonstrate an easily-fabricated and efficient ZnO DSSC anode, i.e., the ZnO NC-NS framework, which is hierarchically constructed on the ZnO NW-array template by a facile RT CBD method within 4 min. The RT-grown ZnO nanostructures provide larger and more fitting surface for dye adsorption. The light scattering ability of the ZnO anode is also enhanced with the RT ZnO nanoarchitectures. The improvement in light-harvesting efficiency by the light-scattering effect and the increase in the dye adsorption results in the considerable enrichment of the J_{sc} in the ZnO NC-NS DSSC. Moreover, with the RT ZnO nanostructures fully covering ZnO NWs, the ZnO NC-NS anode possesses an upward-shifted conduction band edge compared to the ZnO NW anode. The Voc is therefore significantly improved in the ZnO NC-NS DSSC. On the other hand, the RT-grown ZnO nanostructures afford a fast electron transport pathway compared the primary ZnO NWs. With the large surface area, high light-scattering ability, elevated conduction band edge, and fast electron transport rate, the ZnO NC-NS framework has been demonstrated to be an outperformed DSSC anode. With an anode thickness of 9 μm, an efficiency of 5.14% is therefore attained in the D149-sensitized ZnO NC-NS DSSC.

ASSOCIATED CONTENT

Supporting Information

Typical IMPS responses of the ZnO NW and ZnO NC-NS DSSCs as well as the analyses of relative conduction band edges of the ZnO NW-based anodes by EIS. This material is available free of charge via the Internet at http://pubs.acs.org.

AUTHOR INFORMATION

Corresponding Author

*E-mail: wujj@mail.ncku.edu.tw.

Notes

The authors declare no competing financial interest.

ACKNOWLEDGMENTS

The financial support from the National Science Council of Taiwan under grants NSC 99-2221-E-006-198-MY3 and NSC 100-2628-E006-032-MY2 is gratefully acknowledged.

REFERENCES

(1) Zhang, Q.; Dandeneau, C. S.; Zhou, X.; Cao, G. *Adv. Mater.* **2009**, *21*, 4087.
(2) Memarian, N.; Concina, I.; Braga, A.; Rozati, S. M.; Vomiero, A.; Sberveglieri, G. *Angew. Chem., Int. Ed.* **2011**, *50*, 12321.
(3) Yella, A.; Lee, H.-W.; Tsao, H. N.; Yi, C.; Chandiran, A. K.; Nazeeruddin, M. K.; Diau, E. W.-G.; Yeh, C.-Y.; Zakeeruddin, S. M.; Grätzel, M. *Science* **2011**, *334*, 629.
(4) Yoshida, T.; Zhang, J.; Komatsu, D.; Sawatani, S.; Minoura, H.; Pauporté, T.; Lincot, D.; Oekermann, T.; Schlettwein, D.; Tada, H.; Wohrle, D.; Funabiki, K.; Matsui, M.; Miura, H.; Yanagi, H. *Adv. Funct. Mater.* **2008**, *18*, 1.
(5) Anta, J. A.; Guillen, E.; Tena-Zaera, R. *J. Phy. Chem. C* **2012**, *116*, 11413.
(6) Law, M.; Greene, L. E.; Johnson, J. C.; Saykally, R.; Yang, P. D. *Nat. Mater.* **2005**, *4*, 455.
(7) Ku, C.-H.; Wu, J.-J. *Appl. Phys. Lett.* **2007**, *91*, 093117.
(8) Wong, D. K.-P.; Ku, C.-H.; Chen, Y.-R.; Chen, G.-R.; Wu, J.-J. *ChemPhysChem* **2009**, *10*, 2698.
(9) Wu, C.-T.; Liao, W.-P.; Wu, J.-J. *J. Mater. Chem.* **2011**, *21*, 2871.
(10) Wu, J.-J.; Chen, G.-R.; Yang, H.-H.; Ku, C.-H.; Lai, J.-Y. *Appl. Phys. Lett.* **2007**, *90*, 213109.
(11) González-Moreno, R.; Cook, P. L.; Zegkinoglou, I.; Liu, X.; Johnson, P. S.; Yang, W.; Ruther, R. E.; Hamers, R. J.; Tena-Zaera, R.; Himpsel, F. J.; Ortega, J. E.; Rogero, C. *J. Phys. Chem. C* **2011**, *115*, 18195.
(12) Lin, C.-Y.; Lai, Y.-H.; Chen, H.-W.; Chen, J.-G.; Kung, C.-W.; Vittal, R.; Ho, K.-C. *Energy Environ. Sci.* **2011**, *4*, 3448.
(13) Wu, C.-T.; Wu, J.-J. *J. Mater. Chem.* **2011**, *21*, 13605.
(14) Wu, J.-J.; Chen, Y.-R.; Liao, W.-P.; Wu, C.-T.; Chen, C.-Y. *ACS Nano* **2010**, *4*, 5679.
(15) Sung, Y.-H.; Liao, W.-P.; Chen, D.-W.; Wu, C.-T.; Chang, G.-J.; Wu, J.-J. *Adv. Funct. Mater.* **2012**, *22*, 3808.
(16) Pacholski, C.; Kornowski, A.; Weller, H. *Angew. Chem. Int. Ed.* **2002**, *41*, 1188.
(17) Wang, M.; Gratzel, C.; Moon, S.-J.; Humphry-Baker, R.; Rossier-Iten, N.; Zakeeruddin, S. M.; Gratzel, M. *Adv. Funct. Mater.* **2009**, *19*, 2163.
(18) Fabregat-Santiago, F.; Garcia-Belmonte, G.; Mora-Sero', I.; Bisquert, J. *Phys. Chem. Chem. Phys.* **2011**, *13*, 9083.